

1           **Origin and consequences of non-stoichiometry in iron carbide Fe<sub>7</sub>C<sub>3</sub>**

2   FENG ZHU<sup>1,\*</sup>, JIE LI<sup>1</sup>, DAVID WALKER<sup>2</sup>, JIACHAO LIU<sup>1,†</sup>, XIAOJING LAI<sup>3,4</sup>,  
3   DONGZHOU ZHANG<sup>3</sup>

4   <sup>1</sup>Earth and Environmental Sciences, University of Michigan, Ann Arbor, Michigan 48109,  
5   U.S.A.

6   <sup>2</sup>Earth and Environmental Science, LDEO, Columbia University, Palisades, New York  
7   10964, U.S.A.

8   <sup>3</sup>Hawaii Institute of Geophysics and Planetology, University of Hawaii at Manoa,  
9   Honolulu, Hawaii 96822, U.S.A.

10   <sup>4</sup>Department of Geology and Geophysics, University of Hawaii at Manoa, Honolulu,  
11   Hawaii 96822, U.S.A.

12

13   \* Corresponding author:

14   Feng Zhu ([fzhuum@umich.edu](mailto:fzhuum@umich.edu))

15

16   † Current address:

17   Department of Geological Sciences, Jackson School of Geosciences, University of Texas  
18   at Austin, Austin, Texas, 78712, USA

19

**Revision 2**

---

20 **ABSTRACT**

21 The Eckstrom-Adcock iron carbide, nominally  $\text{Fe}_7\text{C}_3$ , is a potential host of reduced  
22 carbon in Earth's mantle and a candidate component of the inner core. Non-stoichiometry  
23 in  $\text{Fe}_7\text{C}_3$  has been observed previously but the crystal chemistry basis for its origin and  
24 influences on the physical properties were not known. Here we report chemical and  
25 structural analyses of synthetic  $\text{Fe}_7\text{C}_3$  that was grown through diffusive reaction between  
26 iron and graphite and contained 31 to 35 at.% carbon. We found that more carbon-rich  
27  $\text{Fe}_7\text{C}_3$  has smaller unit-cell volume, suggesting that excess carbon atoms substituted for  
28 iron atoms instead of entering the interstitial sites of closed-packed iron lattice as in  $\text{FeC}_x$   
29 steel. Carbon may be the lightest alloying element to substitute for iron. The substitution  
30 leads to larger reduction in the unit-cell mass than the volume so that the carbon-rich end  
31 member may be as much as 5% less dense than stoichiometric  $\text{Fe}_7\text{C}_3$ . If  $\text{Fe}_7\text{C}_3$  solidifies  
32 from Earth's iron-rich liquid core, it is expected to have a nearly stoichiometric  
33 composition with a compositional expansion coefficient of  $\sim 1.0$ . However, laboratory  
34 experiments using carbon-rich synthetic  $\text{Fe}_7\text{C}_3$  to model the inner core may over-estimate  
35 the amount of carbon that is needed to account for the core density deficit.

36 **Keywords:** Iron carbide, non-stoichiometry, substitution, interstice, light element,  
37 density deficit, compositional expansion coefficient

38

## 39 INTRODUCTION

40 Eckstrom-Adcock iron carbide ( $\text{Fe}_7\text{C}_3$ ) was first discovered in a hydrocarbon synthesis  
41 plant (Eckstrom and Adcock, 1950).  $\text{Fe}_7\text{C}_3$  is considered a potential host of reduced  
42 carbon in Earth's deep mantle, where metallic iron is expected to be stable (Rohrbach and  
43 Schmidt, 2011). It is also a candidate component to explain the density deficit and  
44 anomalously low shear wave velocity of the inner core (Chen et al., 2012; Chen et al.,  
45 2014; Liu et al., 2016; Prescher et al., 2015).  $\text{M}_7\text{C}_3$  ( $\text{M}_2\text{C}$ )-type intermediate transition-  
46 metal carbides have been found as inclusions in superdeep diamonds together with  
47 cementite  $\text{M}_3\text{C}$ , where M stands for Fe, Co, Ni, Cr, and Mn. These natural  $\text{M}_7\text{C}_3$  ( $\text{M}_2\text{C}$ )  
48 and  $\text{M}_3\text{C}$  samples can have ~6-8 at.% C content variation in the same structure.  
49 (Kaminsky and Wirth, 2011; Smith et al., 2016). Synthetic iron carbides also show  
50 considerable compositional variation, ranging from 29 to 36 at.% carbon in  $\text{Fe}_7\text{C}_3$  and  
51 from 17 to 31 at.% carbon in  $\text{Fe}_3\text{C}$  (Buono et al., 2013; Walker et al., 2013). Deviation  
52 from stoichiometric composition led to a reduction of the Curie temperature of  $\text{Fe}_3\text{C}$   
53 (Walker et al., 2015). Moreover, a carbon-poor  $\text{Fe}_3\text{C}$  was found to have a smaller unit-  
54 cell volume than a slightly carbon-rich phase, suggesting that the carbon deficiency  
55 originates from carbon vacancy. The correlation between volume and composition is  
56 similar to  $\text{FeC}_x$  or  $\text{FeH}_x$  alloys, where unit-cell volume increases with the increasing  
57 amount of light element, and opposite to Fe-O, Fe-Si, and Fe-S alloys where the unit-cell  
58 volume decreases with the increasing amount of light element (Table 1). On the other  
59 hand, the origin and effects of non-stoichiometry on  $\text{Fe}_7\text{C}_3$  are still not known. Here we  
60 investigate the composition and structure of non-stoichiometry in  $\text{Fe}_7\text{C}_3$  through  
61 synchrotron X-ray diffraction (XRD) and electron probe microanalysis (EPMA) and

**Revision 2**

---

62 discuss the implications for the stability and properties of carbides in the deep Earth.

63

64 **METHODS**

65 Non-stoichiometric iron carbide  $\text{Fe}_7\text{C}_3$  was synthesized using a multi-anvil  
66 apparatus at the Lamont-Doherty Earth Observatory (LDEO serial #BB-1233) (Walker et  
67 al., 2013). The starting material consists of a 250- $\mu\text{m}$ -thick iron disc (Goodfellow hard  
68 iron foil, >99.5%) sandwiched between two graphite cylinders (National Carbon  
69 Spectroscopic grade graphite), surrounded by high-purity MgO sleeve. The sample was  
70 contained in an 8 mm truncated edge length (TEL) octahedron of Ceramacast 584  
71 castable ceramic (Aremco) and equilibrated at 7 GPa (350 US ton oil pressure) and 1300  
72 °C for 19 hrs. The temperature difference across the sample is estimated to be <10 °C,  
73 and the pressure uncertainty is estimated to be 0.5 GPa in the sample capsule. The  
74 experimental product was ground to form a 1.8-mm-long, 0.4-mm-tall, and 300- $\mu\text{m}$ -thick  
75 pellet (parallel to the rotation axis of the original Fe disc and C cylinders) that presented  
76 as a sectioned sandwich with carbide as the jelly between carbon bread slices for  
77 synchrotron XRD measurements at 13-BM-C of the Advanced Photon Source (APS),  
78 Argonne National Laboratory (ANL). The X-ray wavelength is 0.4340 ( $\pm 2 \times 10^{-5}$ ) Å and  
79 the beam size is  $12 \times 18 \mu\text{m}^2$  at the full width at half maximum (FWHM)  
80 (horizontal  $\times$  vertical direction in Fig. 1). The sample to detector distance is 164.10 ( $\pm 0.03$ )  
81 mm. The slice was rotated around the original rotation axis of the Fe disc and C cylinders  
82 (stacking direction of the sandwich) by  $\pm 30^\circ$  to reduce the effect of preferred orientation  
83 in the coarse-grained sample. The XRD data were processed using Dioptas (Prescher and  
84 Prakapenka, 2015) and PDIndexer (Seto et al., 2010) software.

**Revision 2**

---

85           After the XRD measurements, the slice was coated with aluminum for electron  
86 microprobe analysis, using the JOEL-7800FLV scanning electron microscope (SEM) and  
87 Cameca SX100 EPMA at the Electron Microbeam Analysis Laboratory (EMAL) of  
88 University of Michigan. No chemical contamination was detected in the SEM and EPMA  
89 measurements. For the EPMA analysis, a 11 kV accelerating voltage and a 70 nA beam  
90 focused to  $\sim 1$   $\mu\text{m}$  diameter was used to obtain compositional data (Dasgupta and Walker,  
91 2008). The penetration depth of the beam was estimated to be  $<20$   $\mu\text{m}$ . Pure Fe and  
92 synthetic stoichiometric  $\text{Fe}_3\text{C}$  were used as the standards (Liu et al., 2016). The  
93 measurement time for the sample was 10 seconds on the peak positions and 5 seconds on  
94 the background.

95

96   **RESULTS AND DISCUSSION**

97   **Anti-correlation between unit-cell volume and carbon content in non-stoichiometric**  
98    **$\text{Fe}_7\text{C}_3$**

99           Back-scattered electron (BSE) image showed that the synthesis experiment  
100 produced two layers of the Eckstrom-Adcock carbide, nominally  $\text{Fe}_7\text{C}_3$ , each sandwiched  
101 between a layer of cementite, nominally  $\text{Fe}_3\text{C}$ , in the center of the sample and unreacted  
102 carbon on both ends (Fig. 1). The layered structure indicates that the C and  $\text{Fe}_3\text{C}$  layers  
103 were not fully equilibrated when the sample was quenched from high temperature. As a  
104 result, ongoing C diffusion from the C layers to  $\text{Fe}_3\text{C}$  layer through the  $\text{Fe}_7\text{C}_3$  layers in  
105 between was preserved in the sample, creating the gradient of C content in the  $\text{Fe}_7\text{C}_3$   
106 layers, which points from the carbon-rich end near the  $\text{Fe}_7\text{C}_3/\text{C}$  boundary to carbon-poor  
107 end near the  $\text{Fe}_7\text{C}_3/\text{Fe}_3\text{C}$  boundary.

Revision 2

---

108           The layered distribution of the three phases was confirmed by XRD line scans  
109 (Fig. 2). The phase assemblies evolve from C+Fe<sub>7</sub>C<sub>3</sub> at the graphite ends to Fe<sub>7</sub>C<sub>3</sub> and  
110 then to Fe<sub>3</sub>C. Some XRD patterns of the Fe<sub>7</sub>C<sub>3</sub> contained variable amounts of Fe<sub>3</sub>C.  
111 Minor Fe<sub>7</sub>C<sub>3</sub> phase was also found in the XRD collected from the Fe<sub>3</sub>C band. The  
112 occurrence of both carbides in the XRD patterns collected from the interior of different  
113 bands appears inconsistent with the clear separation of the bands in the BSE and optical  
114 images. We found that on the exiting side of the X-ray beam the center Fe<sub>3</sub>C band is 40  
115 μm thinner, suggesting that the boundaries between Fe<sub>7</sub>C<sub>3</sub> and Fe<sub>3</sub>C are not parallel and  
116 therefore the beam that enters the sample near the interface would traverse both phases.  
117 This effect is enhanced considering that 25% of X-ray intensity is outside the FWHM and  
118 can produce diffraction signals from 40-micron areas. It is also possible that the stacking  
119 direction of sample is slightly tilted towards or away from the X-ray beam direction and  
120 therefore XRD patterns containing single carbide are only collected from measurements  
121 near the center of each band, as we observed.

122           Despite these complications, a unit-cell volume composite map constructed from the  
123 XRD line scans revealed a general trend that Fe<sub>7</sub>C<sub>3</sub> closer to the carbon layer has smaller  
124 unit-cell volume (Fig. 3). We used hexagonal structure (*P6<sub>3</sub>mc*) (Herbstein and Snyman,  
125 1964) to refine the structure of Fe<sub>7</sub>C<sub>3</sub> since it better explained the observed patterns. Six  
126 fixed peaks (112), (031), (022), (220), (033) and (232) which have no overlap with Fe<sub>3</sub>C  
127 strong peaks were used for the refinement of all present unit-cell volumes to avoid  
128 complications, and the largest unit-cell of Fe<sub>7</sub>C<sub>3</sub> was found in the Fe<sub>3</sub>C center band,  
129 where Fe<sub>7</sub>C<sub>3</sub> occurred as a minor phase in the mixed XRD patterns. The trend of  
130 decreasing volume towards the carbon layer is further confirmed by the stacked XRD

**Revision 2**

---

131 patterns showing a systematic shift of peak position towards larger  $2\theta$  as the X-ray beam  
132 moved from the  $\text{Fe}_3\text{C}$ - $\text{Fe}_7\text{C}_3$  boundary towards the  $\text{Fe}_7\text{C}_3$ -C boundary (Fig. 4).  $\text{Fe}_3\text{C}$   
133 exhibits a similar correlation of higher carbon content with smaller unit-cell volume,  
134 although there is considerable scatter and the trend is not as well resolved (Fig. 4a&d).  
135 These peak shifts, although only  $\sim 0.02^\circ$ , are much larger than the potential shifts caused  
136 by uncertainties in X-ray wavelength ( $0.0006^\circ$  at  $2\theta \sim 14^\circ$  corresponding to 1 eV energy  
137 fluctuation) and sample-to-detector distance ( $0.0024^\circ$  at  $2\theta \sim 14^\circ$  corresponding to 30  $\mu\text{m}$   
138 sample distance variation). The sample-detector distance at the center band of  $\text{Fe}_3\text{C}$   
139 + $\text{Fe}_7\text{C}_3$  mixture can differ by up to  $\sim 100 \mu\text{m}$  from the  $\text{Fe}_7\text{C}_3$  band at the edge.  
140 Accordingly, the  $2\theta$  could shift up to  $0.008^\circ$  and may have visible influence on the unit-  
141 cell volumes of the center-most  $\text{Fe}_7\text{C}_3$ , but not enough to account for the total observed  
142 shift. Additionally, the peak shift was observed in  $\text{Fe}_7\text{C}_3$  phase at the edge free of  $\text{Fe}_3\text{C}$   
143 (Fig. 4c), thus ruling out the possibility that the  $2\theta$  shift mainly comes from phase  
144 mixture. In all seven line scans the largest volumes appear in the center, suggesting that  
145 the  $2\theta$  shift does not come from random fluctuation. Therefore, the variation in cell  
146 volume suggests non-stoichiometry in  $\text{Fe}_3\text{C}$  and  $\text{Fe}_7\text{C}_3$ . More importantly, the data  
147 suggest an anti-correlation between cell volume and carbon content: As the carbon  
148 concentration increases, the cell volume became smaller.

149 EPMA line scans showed two clusters of composition at  $\sim 24$ - $27$  at.% and  $\sim 31$ - $35$  at.%  
150 carbon, corresponding to  $\text{Fe}_3\text{C}$  and  $\text{Fe}_7\text{C}_3$ , respectively (Fig. 5). The ranges of non-  
151 stoichiometry agree with the previous studies (Buono et al., 2013; Walker et al., 2013).  
152 The compositions of  $\text{Fe}_3\text{C}$  mostly fell on the carbon-rich side of the stoichiometric  
153 compound, consistent with the fact that the iron in the starting material was fully

**Revision 2**

---

154 consumed and the product still contains unreacted carbon. Overall the carbon content  
155 decreases from the region next to unreacted carbon towards that next to the Fe<sub>3</sub>C band,  
156 consistent with the direction of C diffusion (Fig. 5). Compositional fluctuation exists in  
157 individual line scan, especially Line A near the distal edge, due to the complexity in  
158 carbon diffusion (Walker et al., 2013) and the large uncertainty in measuring C  
159 concentration by EPMA.

160       Compared with EPMA measurements, less fluctuation of unit-cell volume was  
161 observed in XRD (Fig. 3 and Fig. 5). This is mainly because the sample volume covered  
162 by XRD is significantly larger than that by EPMA (12×18 μm beam size and 300 μm  
163 depth in XRD compared with ~1 μm beam size and <20 μm penetration depth in EPMA).  
164 With thousands of times volume coverage, together with the sample rotation, the XRD  
165 measurements effectively reduced the scattering caused by complexity of local  
166 composition and obtained the average lattice parameters for the covered volume.

167       From the most carbon-rich part with 35 at.% carbon to the least carbon-rich part  
168 with 31 at.% carbon in the Fe<sub>7</sub>C<sub>3</sub> band, the unit-cell volume expands by ~0.3% from  
169 ~186.2 Å<sup>3</sup> to 186.8 Å<sup>3</sup>. Larger unit-cell volume up to ~187.4 Å<sup>3</sup> was obtained from the  
170 Fe<sub>7</sub>C<sub>3</sub>-Fe<sub>3</sub>C mixture in the center band, where carbon content may be lower than 31 at.%  
171 and the XRD beam averaged less volume from carbon-rich Fe<sub>7</sub>C<sub>3</sub> when it crossed the  
172 Fe<sub>7</sub>C<sub>3</sub>-Fe<sub>3</sub>C phase boundary. Because large uncertainty may exist in both the composition  
173 and volume refinement in this phase mixture region, it is excluded from the latter density  
174 calculation.

175

176 **Origin of non-stoichiometry in Fe<sub>7</sub>C<sub>3</sub> and Fe<sub>3</sub>C**



**Revision 2**

---

177 The composition-volume relation of iron carbides can be used to infer the  
178 mechanism by which carbon is removed or added from the structures of stoichiometric  
179 compounds. Cementite  $\text{Fe}_3\text{C}$  is usually considered an interstitial alloy, in which carbon  
180 atoms adopt the six-fold interstitial sites of iron in *hcp* structure (Barrett, 1943; Scott et  
181 al., 2001). First-principles calculations found that carbon enters the interstitial sites of  
182 closed packed structure of iron and therefore adding a small amount of carbon ( $x < 0.1$ )  
183 to *hcp* Fe expands the lattice (Caracas, 2017). The interstitial model, however, cannot  
184 explain the smaller volumes of carbon-rich  $\text{Fe}_7\text{C}_3$  and  $\text{Fe}_3\text{C}$ , suggesting that carbon-iron  
185 substitution may be the cause of carbon-rich carbides.

186 By contrast, Walker et al. (2013) found that the unit-cell volume of a carbon-poor  
187  $\text{Fe}_3\text{C}$  with 22.3 at% carbon is smaller than that of a slightly carbon-rich  $\text{Fe}_3\text{C}$  with 25.6 at%  
188 carbon. Petch (1944) also found that volume decreases with decreasing C content in Fe-  
189 saturated cementites as they become less stoichiometric and C-poorer with rising  
190 temperature. Results from the two literature studies on C-poor cementite, compared to the  
191 present study of C-rich cementite therefore suggest that deviation from the stoichiometric  
192 composition of  $\text{Fe}_3\text{C}$  in either direction reduces the cell volume and that the mechanisms  
193 of non-stoichiometry may be different on different sides of stoichiometric  $\text{Fe}_3\text{C}$ . In light  
194 of this new evidence, the supposition of Walker et al. (2015) that the non-stoichiometry  
195 mechanism on the C-rich side of  $\text{Fe}_3\text{C}$  is interstitial, is less plausible than that it is  
196 substitutional. Walker et al. (2015) found that the Curie temperature is lower on either  
197 side of  $\text{Fe}_3\text{C}$  but the rate of  $T_c$  reduction on the C-rich side is twice that on the C-poor  
198 side. They attributed the rate differences to larger configurational entropy production by  
199 interstitial C on the C-rich side than by C vacancy on the C-poor side. We now regard

**Revision 2**

---

200 substitutional C as a more plausible mechanism on the C-rich side on the basis of the new  
201 evidence presented here. The entropy argument, however remains unchanged because  
202 there are still twice as many sites for substitution on the C-rich side as there are for C  
203 vacancy on the C-poor side of Fe<sub>3</sub>C. The entropy production rate in this particular case is  
204 insensitive to compositional variation mechanism for introducing C richness.

205 A closer look at the structures of Fe<sub>3</sub>C and Fe<sub>7</sub>C<sub>3</sub> reveal that carbon takes a distinct  
206 8-fold square antiprism site instead of the interstitial sites of close-packed iron lattice (Fig.  
207 6). The presence of carbon distorts the 6-fold interstitial sites and enlarges the lattice. As  
208 a result, 2/3 of the iron atoms in Fe<sub>3</sub>C and 6/7 of that in Fe<sub>7</sub>C<sub>3</sub> have only 11 nearest iron  
209 neighbors and the sub-structures of iron atoms are no longer ideal *hcp* closest packing.  
210 The 8-fold carbon sites and 11-fold iron sites in the carbide structures can be explained  
211 by the nature of metallic bonding between carbon and iron, where carbon acts as an  
212 electron donor and enhances the hybridization between the partially filled 3d orbital and  
213 the 4s orbital of iron (Goldschmidt, 1967). As a result, C in iron carbides should be  
214 treated as C<sup>0</sup>, instead of C<sup>4-</sup> as in covalent and stoichiometric compounds such as SiC,  
215 Al<sub>4</sub>C<sub>3</sub> and Mg<sub>2</sub>C. For metallic bonding between Fe<sup>0</sup> and C<sup>0</sup> the radius ratio  $r_C/r_{Fe}$  is ~0.62  
216 or slightly larger with corrections for electronegativity of Fe (1.83) and C (2.55) (Allred,  
217 1961). According to Pauling's rules this ratio is slightly too high for carbon to take the 6-  
218 fold interstitial site ( $r_A/r_X = 0.414$ ) and too low for C-Fe substitution ( $r_A/r_X = 1$ ).  
219 Consequently, only a small amount of interstitial carbon is allowed in FeC<sub>x</sub> alloys.  
220 Carbon in Fe<sub>3</sub>C and Fe<sub>7</sub>C<sub>3</sub> adopts 8-fold square antiprism sites ( $r_C/r_a = 0.645$  in Pauling's  
221 rules) instead of entering the interstices of close-packed iron.

222 Because carbon adopts an 8-fold site that is not much smaller than 11-fold iron sites,

**Revision 2**

---

223 excess carbon atoms in  $\text{Fe}_3\text{C}$  and  $\text{Fe}_7\text{C}_3$  may be incorporated into the structure through  
224 substitution of carbon for iron (Fig. 6). This substitution explains the reduced volumes of  
225 carbon-rich  $\text{Fe}_3\text{C}$  and  $\text{Fe}_7\text{C}_3$ . No carbon-poor  $\text{Fe}_7\text{C}_3$  has been found in this study or  
226 previous synthesis (Walker et al., 2013), suggesting that it is less stable than a two-phase  
227 mixture of  $\text{Fe}_3\text{C}$  and stoichiometric  $\text{Fe}_7\text{C}_3$ .

228 The inferred origin of non-stoichiometry in carbon-poor and carbon-rich  $\text{Fe}_3\text{C}$  is  
229 consistent with the relations between the lattice parameters and carbon content. An anti-  
230 correlation in lattice parameters was reported in C-poor  $\text{Fe}_3\text{C}$  such that the  $b$  axis  
231 elongates with decreased C content while the unit-cell volume (and  $a$ ,  $c$  axes) shrinks  
232 (Petch, 1944; Walker et al., 2013). This kind of anti-correlation was not observed in the  
233 C-rich  $\text{Fe}_3\text{C}$  in this study. For example, in Line 1 the maximum unit-cell volume of  $\text{Fe}_3\text{C}$   
234 is  $155.93(27) \text{ \AA}^3$  with  $a = 5.098(2) \text{ \AA}$ ,  $b = 6.760(4) \text{ \AA}$  and  $c = 4.525(2) \text{ \AA}$ , and the  
235 minimum unit-cell volume is  $155.47(38) \text{ \AA}^3$  with  $a = 5.094(2) \text{ \AA}$ ,  $b = 6.748(7) \text{ \AA}$  and  $c =$   
236  $4.523(3) \text{ \AA}$ . Carbon in the antiprism site of  $\text{Fe}_3\text{C}$  introduces pleats to the close-packed Fe  
237 in  $b$  direction, which changes the folding angle of the pleats from  $180^\circ$  (no folding) to  
238  $\sim 120^\circ$ . The carbon vacancy unbends the pleats in the  $b$  direction and lets them stack  
239 better in  $a$  and  $c$  direction, thus increasing the axial length in the  $b$  direction and  
240 decreasing it in the  $a/c$  direction. On the C-rich side, all the antiprism sites are filled and  
241 the excess carbon takes the Fe site instead. Because there is no further occupancy of the  
242 antiprism sites, the anti-correlation between  $b$  and unit-cell volume disappears on the C-  
243 rich side.

244 The inferred site occupancy is further corroborated by the diffusion rates of carbon  
245 and iron in  $\text{FeC}_x$  alloy and iron carbides. Carbon diffusion in austenite and ferrite is

**Revision 2**

---

246 considered a typical example of rapid interstitial diffusion, whereas self-diffusion of iron  
247 is a typical example of substitution (vacancy) diffusion. At 1 bar and 1000 K, the  
248 diffusion coefficient of carbon in  $\text{Fe}_3\text{C}$  is  $\sim 10^{-15} \text{ m}^2/\text{s}$ , which falls between that of carbon  
249 in *bcc* Fe ( $\sim 10^{-10} \text{ m}^2/\text{s}$ ) or *fcc* Fe ( $\sim 10^{-12} \text{ m}^2/\text{s}$ ) and that of iron in *bcc* Fe ( $\sim 10^{-17} \text{ m}^2/\text{s}$ ) or  
250 *fcc* Fe ( $\sim 10^{-19} \text{ m}^2/\text{s}$ ) (Gale and Totemeier, 2003; Hillert et al., 2005; Ozturk et al., 1984).  
251 The intermediate value of diffusion coefficient suggests that carbon in  $\text{Fe}_3\text{C}$  cannot be  
252 treated as an interstitial constituent. Molecular dynamics simulations suggest that six-fold  
253 interstitial sites may serve as transient “stepping stones” to facilitate diffusion of carbon  
254 among anti-prismatic sites (Levchenko et al., 2009). This interstice-assisted diffusion  
255 mechanism implies carbon diffusion in  $\text{Fe}_3\text{C}$  may include both interstitial and  
256 substitutional mechanism, and the substitutional diffusion is likely the rate-limiting step  
257 that caused the observed gradient non-stoichiometry in the diffusive reaction product in  
258 this study.

259 The roughly planar boundaries between  $\text{Fe}_3\text{C}$ ,  $\text{Fe}_7\text{C}_3$ , and C in the recovered samples  
260 synthesized at 7 GPa from this and previous study suggested that the reactions were  
261 controlled mainly by lattice diffusion, without significant transport along grain  
262 boundaries (Walker et al., 2013). The widths of  $\text{Fe}_3\text{C}$  layer and  $\text{Fe}_7\text{C}_3$  layer in either this  
263 study or the previous study are comparable, thus indicating the lattice diffusion rates of  
264 carbon in  $\text{Fe}_7\text{C}_3$  and  $\text{Fe}_3\text{C}$  are similar, which in turn implies the same origin of non-  
265 stoichiometry on the carbon-rich sides of these carbides.

266

267 **Density of non-stoichiometric iron-light element alloys**

268 The density of an iron carbide may be calculated from its unit-cell volume from

Revision 2

---

269 XRD measurements and the composition as determined by microprobe analysis only if  
270 we can infer the mechanism of non-stoichiometry. For a carbon-rich  $\text{Fe}_7\text{C}_3$  with 35 at.%  
271 carbon, the formula unit may be written as  $\text{Fe}_{6.5}\text{C}_{3.5}$  for a substitution alloy or  $\text{Fe}_7\text{C}_{3.77}$  for  
272 an interstitial alloy. Depending on the mechanism of non-stoichiometry, the calculated  
273 densities for the same unit-cell volume and chemical composition could differ by more  
274 than 5% (Table 1). It is therefore important to understand the nature of non-stoichiometry.

275 The presence of a light element in an iron-alloy usually reduces its density. The  
276 efficiency of density reduction can be described by the compositional expansion  
277 coefficient  $\alpha_c$ , the ratio between the relative density reduction and the concentration of  
278 the light element in weight percent. With respect to *hcp* iron, the  $\alpha_c$  of stoichiometric  
279  $\text{Fe}_3\text{C}$  and  $\text{Fe}_7\text{C}_3$  is 1.4, corresponding to 1.4% density reduction for 1 wt.% of carbon in  
280 the Fe-alloy (Fig. 7). Carbon excess in  $\text{Fe}_7\text{C}_3$  leads to a local excursion of  $\alpha_c$  to 2.6,  
281 because replacing iron with carbon reduces the cell mass much more than the cell volume.  
282 It is interesting to note that carbon vacancy in  $\text{Fe}_3\text{C}$  may give rise to local negative  $\alpha_c$   
283 with respect to stoichiometric composition: Between carbon-poor  $\text{Fe}_3\text{C}$  with vacancy and  
284 nearly stoichiometric  $\text{Fe}_3\text{C}$ , the local  $\alpha_c$  is -0.9 (Fig. 7, Table 1).

285 Non-stoichiometry is common among iron-light-element alloys and may cause  
286 variations in compositional expansion coefficient (Fig. 8). At ambient conditions,  
287 however, the complexity in calculating density from measured cell volume and  
288 composition may be applicable to carbon alone. This is because the atomic or covalent  
289 radius of carbon makes a borderline case for it to act as an interstitial constituent as in  
290  $\text{FeC}_x$ , or as a substituent of iron as in carbon-rich  $\text{Fe}_3\text{C}$  and  $\text{Fe}_7\text{C}_3$ . With  $r_{\text{H}}/r_{\text{Fe}} \sim 0.29$ ,  
291  $\text{FeH}_x$  is considered a typical interstitial alloy. Silicon is comparable to iron in size ( $r_{\text{Si}}/r_{\text{Fe}}$

**Revision 2**

---

292 ~0.94) and electronegativity and therefore all Fe-Si alloys are substitutional. Oxygen and  
293 sulfur are highly electro-negative and their anions are much larger than an iron cation,  
294 and therefore iron vacancy is the dominant mechanism for non-stoichiometry in  $\text{Fe}_{1-x}\text{O}$   
295 (Hazen and Jeanloz, 1984) and  $\text{Fe}_{1-x}\text{S}$  (Palache et al., 1944). At high pressures,  $\text{Fe}_{1-x}\text{S}_x$  ( $x$   
296  $< 0.1$ ) solutions have been predicted and observed (Alfe et al., 2002; Kamada et al., 2012;  
297 Kamada et al., 2010; Li et al., 2001). Pressure may influence the electronegativity and  
298 radii of iron and sulfur differently, hence it may be necessary to examine the dissolution  
299 mechanism of sulfur in iron in order to correctly calculate the density of Fe-S alloys at  
300 high pressures.

301

## 302 **IMPLICATIONS**

303 As a candidate component of the Earth's inner core,  $\text{Fe}_7\text{C}_3$  is likely nearly  
304 stoichiometric because it solidifies from the outer core which contains at least 85 wt.%  
305 iron. In recent mineral physics experiments,  $\text{Fe}_7\text{C}_3$  samples are often synthesized in  
306 graphite capsules and therefore carbon-saturated (Chen et al., 2014; Nakajima et al., 2011;  
307 Prescher et al., 2015). In these studies, the density of  $\text{Fe}_7\text{C}_3$  was calculated by assuming  
308 stoichiometric composition because non-stoichiometry was not widely recognized at the  
309 time, and the exact compositions of micrometer sized samples used for the diamond-anvil  
310 cell measurements were not readily accessible. The calculated density of synthetic C-rich  
311  $\text{Fe}_7\text{C}_3$  could be as much as 1.2% larger than nearly stoichiometric  $\text{Fe}_7\text{C}_3$  in the core, and  
312 therefore, the mass fraction of  $\text{Fe}_7\text{C}_3$  that is needed to account for the density deficit of  
313 the inner core was likely over-estimated by ~6%.

314 The above discussion assumes that the range of non-stoichiometry in  $\text{Fe}_7\text{C}_3$

**Revision 2**

---

315 determined here at 7 GPa and 1300 °C applies at deep mantle or inner core conditions.  
316 The higher temperatures in the deep mantle likely make possible larger deviations from  
317 stoichiometry (Buono et al., 2013; Walker et al., 2013). Pressure and/or temperature  
318 induced exchanges in the compositions of non-stoichiometric iron carbides may lead to  
319 consumption or production of diamonds during downwelling or upwelling processes and  
320 influence chemical equilibrium in deep Earth.

321 Non-stoichiometry is common in iron-rich alloys and may influence the density,  
322 sound velocity, and other physical properties. Further studies are needed to quantify the  
323 effects of pressure and temperature on non-stoichiometry of iron-rich alloys at relevant  
324 conditions and explore the implications for the light element composition of the core.

325

326 **ACKNOWLEDGMENTS**

327 The XRD experiment was performed at GeoSoilEnviroCARS (The University of Chicago,  
328 Sector 13), Advanced Photon Source (APS), Argonne National Laboratory.  
329 GeoSoilEnviroCARS is supported by the National Science Foundation (NSF) - Earth  
330 Sciences (EAR - 1634415) and Department of Energy (DOE) - GeoSciences (DE-FG02-  
331 94ER14466). This research used resources of APS, a U.S. DOE Office of Science User  
332 Facility operated for the DOE Office of Science by Argonne National Laboratory under  
333 Contract No. DE-AC02-06CH11357. This work was partially supported by Sloan  
334 Foundation Grant G-2016-7157, NSF EAR 1763189, and NSF AST 1344133.

335 **REFERENCES CITED**

- 336 Ahrens, L.H. (1952) The use of ionization potentials Part 1. Ionic radii of the elements.  
337 *Geochimica et cosmochimica Acta*, 2(3), 155-169.
- 338 Alfe, D., Gillan, M., and Price, G. (2002) Ab initio chemical potentials of solid and liquid  
339 solutions and the chemistry of the Earth's core. *The Journal of chemical physics*,  
340 116(16), 7127-7136.
- 341 Allred, A. (1961) Electronegativity values from thermochemical data. *Journal of*  
342 *inorganic and nuclear chemistry*, 17(3-4), 215-221.
- 343 Barrett, C.S. (1943) *Structure of metals*. McGraw-Hill Book Company, Inc.; New York.
- 344 Buono, A.S., Dasgupta, R., Lee, C.-T.A., and Walker, D. (2013) Siderophile element  
345 partitioning between cohenite and liquid in the Fe–Ni–S–C system and  
346 implications for geochemistry of planetary cores and mantles. *Geochimica et*  
347 *Cosmochimica Acta*, 120, 239-250.
- 348 Caracas, R. (2017) The influence of carbon on the seismic properties of solid iron.  
349 *Geophysical Research Letters*, 44(1), 128-134.
- 350 Chen, B., Gao, L., Lavina, B., Dera, P., Alp, E.E., Zhao, J., and Li, J. (2012) Magneto-  
351 elastic coupling in compressed Fe<sub>7</sub>C<sub>3</sub> supports carbon in Earth's inner core.  
352 *Geophysical Research Letters*, 39(18).
- 353 Chen, B., Li, Z., Zhang, D., Liu, J., Hu, M.Y., Zhao, J., Bi, W., Alp, E.E., Xiao, Y., and  
354 Chow, P. (2014) Hidden carbon in Earth's inner core revealed by shear softening  
355 in dense Fe<sub>7</sub>C<sub>3</sub>. *Proceedings of the National Academy of Sciences*, 111(50),  
356 17755-17758.
- 357 Dasgupta, R., and Walker, D. (2008) Carbon solubility in core melts in a shallow magma



Revision 2

---

- 358 ocean environment and distribution of carbon between the Earth's core and the  
359 mantle. *Geochimica et Cosmochimica Acta*, 72(18), 4627-4641.
- 360 Eckstrom, H.C., and Adcock, W.A. (1950) A new iron carbide in hydrocarbon synthesis  
361 catalysts. *Journal of the American Chemical Society*, 72(2), 1042-1043.
- 362 Fei, Y., Murphy, C., Shibazaki, Y., Shahar, A., and Huang, H. (2016) Thermal equation  
363 of state of hcp-iron: Constraint on the density deficit of Earth's solid inner core.  
364 *Geophysical Research Letters*, 43(13), 6837-6843.
- 365 Gale, W.F., and Totemeier, T.C. (2003) *Smithells metals reference book*. Butterworth-  
366 Heinemann.
- 367 Goldschmidt, H.J. (1967) Carbides. *Interstitial Alloys*, p. 88-213. Springer.
- 368 Hazen, R.M., and Jeanloz, R. (1984) Wüstite (Fe<sub>1-x</sub>O): A review of its defect structure  
369 and physical properties. *Reviews of Geophysics*, 22(1), 37-46.
- 370 Herbstein, F., and Snyman, J. (1964) Identification of Eckstrom-Adcock iron carbide as  
371 Fe<sub>7</sub>C<sub>3</sub>. *Inorganic Chemistry*, 3(6), 894-896.
- 372 Hillert, M., Höglund, L., and Ågren, J. (2005) Diffusion in interstitial compounds with  
373 thermal and stoichiometric defects. *Journal of applied physics*, 98(5), 053511.
- 374 Hull, A. (1917) Crystal structure of alpha-iron. *Physical Review*, 10, 661-696.
- 375 Kamada, S., Ohtani, E., Terasaki, H., Sakai, T., Miyahara, M., Ohishi, Y., and Hirao, N.  
376 (2012) Melting relationships in the Fe–Fe<sub>3</sub>S system up to the outer core  
377 conditions. *Earth and Planetary Science Letters*, 359, 26-33.
- 378 Kamada, S., Terasaki, H., Ohtani, E., Sakai, T., Kikegawa, T., Ohishi, Y., Hirao, N., Sata,  
379 N., and Kondo, T. (2010) Phase relationships of the Fe–FeS system in conditions

**Revision 2**

---

- 380 up to the Earth's outer core. *Earth and Planetary Science Letters*, 294(1-2), 94-100.
- 381 Kaminsky, F.V., and Wirth, R. (2011) Iron carbide inclusions in lower-mantle diamond  
382 from Juina, Brazil. *The Canadian Mineralogist*, 49(2), 555-572.
- 383 Koto, K., Morimoto, N., and Gyobu, A. (1975) The superstructure of the intermediate  
384 pyrrhotite. I. Partially disordered distribution of metal vacancy in the 6C type,  
385 Fe<sub>11</sub>S<sub>12</sub>. *Acta Crystallographica Section B: Structural Crystallography and*  
386 *Crystal Chemistry*, 31(12), 2759-2764.
- 387 Levchenko, E., Evteev, A., Belova, I., and Murch, G. (2009) Molecular dynamics  
388 simulation and theoretical analysis of carbon diffusion in cementite. *Acta*  
389 *Materialia*, 57(3), 846-853.
- 390 Li, J., Fei, Y., Mao, H., Hirose, K., and Shieh, S. (2001) Sulfur in the Earth's inner core.  
391 *Earth and Planetary Science Letters*, 193(3-4), 509-514.
- 392 Liu, J., Li, J., and Ikuta, D. (2016) Elastic softening in Fe<sub>7</sub>C<sub>3</sub> with implications for  
393 Earth's deep carbon reservoirs. *Journal of Geophysical Research: Solid Earth*,  
394 121(3), 1514-1524.
- 395 Lord, O., Walter, M., Dasgupta, R., Walker, D., and Clark, S. (2009) Melting in the Fe–C  
396 system to 70 GPa. *Earth and Planetary Science Letters*, 284(1), 157-167.
- 397 Machová, A., and Kadečková, S. (1977) Elastic constants of iron-silicon alloy single  
398 crystals. *Czechoslovak Journal of Physics B*, 27(5), 555-563.
- 399 Nakajima, Y., Takahashi, E., Suzuki, T., and Funakoshi, K.-i. (2009) “Carbon in the core”  
400 revisited. *Physics of the Earth and Planetary Interiors*, 174(1), 202-211.
- 401 Nakajima, Y., Takahashi, E., Sata, N., Nishihara, Y., Hirose, K., Funakoshi, K.-i., and  
402 Ohishi, Y. (2011) Thermoelastic property and high-pressure stability of Fe<sub>7</sub>C<sub>3</sub>:

Revision 2

---

- 403           Implication for iron-carbide in the Earth's core. *American Mineralogist*, 96(7),  
404           1158-1165.
- 405 Nakano, A., Tokonami, M., and Morimoto, N. (1979) Refinement of 3C pyrrhotite,  
406           Fe<sub>7</sub>S<sub>8</sub>. *Acta Crystallographica Section B: Structural Crystallography and Crystal*  
407           *Chemistry*, 35(3), 722-724.
- 408 Ohtani, E., Shibazaki, Y., Sakai, T., Mibe, K., Fukui, H., Kamada, S., Sakamaki, T., Seto,  
409           Y., Tsutsui, S., and Baron, A.Q. (2013) Sound velocity of hexagonal close-packed  
410           iron up to core pressures. *Geophysical Research Letters*, 40(19), 5089-5094.
- 411 Okamoto, H. (1992) The C-Fe (carbon-iron) system. *Journal of Phase Equilibria*, 13(5),  
412           543-565.
- 413 Ozturk, B., Fearing, V., Ruth, J., and Simkovich, G. (1984) The diffusion coefficient of  
414           carbon in cementite, Fe<sub>3</sub>C, at 450 C. *Solid State Ionics*, 12, 145-151.
- 415 Palache, C., Berman, H., and Frondel, C. (1944) *The System of Mineralogy*, vol. I—  
416           elements, sulfides, sulfosalts and oxides. New York, 254.
- 417 Pauling, L. (1960) *The Nature of the Chemical Bond*. Cornell university press Ithaca, NY.
- 418 Petch, N. (1944) The interpretation of the crystal structure of cementite. *Journal of the*  
419           *Iron and Steel Institute*, 149, 143-150.
- 420 Prescher, C., Dubrovinsky, L., Bykova, E., Kuppenko, I., Glazyrin, K., Kantor, A.,  
421           McCammon, C., Mookherjee, M., Nakajima, Y., and Miyajima, N. (2015) High  
422           Poisson's ratio of Earth's inner core explained by carbon alloying. *Nature*  
423           *Geoscience*, 8(3), 220.
- 424 Prescher, C., and Prakapenka, V.B. (2015) DIOPTAS: a program for reduction of two-  
425           dimensional X-ray diffraction data and data exploration. *High Pressure Research*,

**Revision 2**

---

- 426           35(3), 223-230.
- 427 Rohrbach, A., and Schmidt, M.W. (2011) Redox freezing and melting in the Earth's deep  
428           mantle resulting from carbon-iron redox coupling. *Nature*, 472(7342), 209-212.
- 429 Routbort, J., Reid, C., Fisher, E., and Dever, D. (1971) High-temperature elastic  
430           constants and the phase stability of silicon-iron. *Acta Metallurgica*, 19(12), 1307-  
431           1316.
- 432 Scott, H.P., Williams, Q., and Knittle, E. (2001) Stability and equation of state of Fe<sub>3</sub>C to  
433           73 GPa: Implications for carbon in the Earth's core. *Geophysical Research Letters*,  
434           28(9), 1875-1878.
- 435 Seto, Y., Nishio-Hamane, D., Nagai, T., and Sata, N. (2010) Development of a software  
436           suite on X-ray diffraction experiments. *Review of High Pressure Science and*  
437           *Technology*, 20(3).
- 438 Smith, E.M., Shirey, S.B., Nestola, F., Bullock, E.S., Wang, J., Richardson, S.H., and  
439           Wang, W. (2016) Large gem diamonds from metallic liquid in Earth's deep  
440           mantle. *Science*, 354(6318), 1403-1405.
- 441 Walker, D., Dasgupta, R., Li, J., and Buono, A. (2013) Nonstoichiometry and growth of  
442           some Fe carbides. *Contributions to Mineralogy and Petrology*, 166(3), 935-957.
- 443 Walker, D., Li, J., Kalkan, B., and Clark, S.M. (2015) Thermal, compositional, and  
444           compressional demagnetization of cementite. *American Mineralogist*, 100(11-12),  
445           2610-2624.
- 446

**Revision 2**

---

447 **FIGURE CAPTIONS**

448 **Figure 1.** Back scattered electron (BSE) image of the diffusive reaction product  
449 consisting of two layers of  $\text{Fe}_7\text{C}_3$  (gray), each sandwiched between graphite (C, dark) and  
450  $\text{Fe}_3\text{C}$  (light gray). The white and black arrows mark the positions of the XRD and EPMA  
451 line scans analyses, respectively. The sample was rotated around the stacking direction of  
452 the sandwich, as indicated by the curved arrow.

453

454 **Figure 2.** Representative XRD patterns collected during line scan. The pattern of the  
455 center  $\text{Fe}_3\text{C}$  band (lower) contains a minor amount of  $\text{Fe}_7\text{C}_3$ . The interior of the  $\text{Fe}_7\text{C}_3$  band  
456 (middle) is pure phase. Diamond, graphite and  $\text{Fe}_7\text{C}_3$  are found in the upper pattern  
457 collected from the C/ $\text{Fe}_7\text{C}_3$  boundary.

458

459 **Figure 3.** Composite map constructed from seven line scans at 30- $\mu\text{m}$  step. The largest  
460 unit-cell volume of  $\text{Fe}_7\text{C}_3$  was found in the center of the sample where  $\text{Fe}_7\text{C}_3$  co-exists  
461 with  $\text{Fe}_3\text{C}$ . The smallest volume is near the edge where  $\text{Fe}_7\text{C}_3$  phase coexists with  
462 unreacted carbon. The  $\text{Fe}_7\text{C}_3$  in the center may have C concentration lower than 31 at.%.

463

464 **Figure 4.** Stacked XRD patterns from line scans. (a) Overall patterns showing that as the  
465 X-ray beam moved towards carbon-rich areas, the  $\text{Fe}_7\text{C}_3$  peaks grew at the expense of the  
466  $\text{Fe}_3\text{C}$  peaks, and both  $\text{Fe}_7\text{C}_3$  and  $\text{Fe}_3\text{C}$  peaks shifted to higher  $2\theta$  (blue and red arrows). (b)  
467 The  $\text{Fe}_7\text{C}_3$  (022) peaks in a series of XRD patterns collected from C- $\text{Fe}_7\text{C}_3$  interface  
468 (black, high carbon) to  $\text{Fe}_7\text{C}_3$ - $\text{Fe}_3\text{C}$  interface (light gray, low carbon content). (c) The  
469  $\text{Fe}_7\text{C}_3$  (121) peaks in several XRD patterns collected from the interior of the  $\text{Fe}_7\text{C}_3$  layer

Revision 2

---

470 free of Fe<sub>3</sub>C peaks shifted to higher  $2\theta$  as the carbon content increased. (d) Overall  
471 patterns of Line 1 at the distant edge, where the variation of carbon content is less than  
472 that in the central positions. Both Fe<sub>7</sub>C<sub>3</sub> and Fe<sub>3</sub>C peaks still shifted to higher  $2\theta$  as the X-  
473 ray beam moved towards carbon-rich areas.

474

475 **Figure 5.** EPMA line scans showing compositional variations in Fe<sub>3</sub>C and Fe<sub>7</sub>C<sub>3</sub> and  
476 carbon gradient in Fe<sub>7</sub>C<sub>3</sub>. Line A in the distal edge has less variation than Line C in the  
477 central position, consistent with Walker et al. (2013).

478

479 **Figure 6.** (a) Structure model of Fe<sub>7</sub>C<sub>3</sub> (*P6<sub>3</sub>mc*) with locally close-packed iron atoms  
480 (dashed circle); (b) CFe<sub>8</sub> polyhedron, which can be viewed as a distorted square antiprism  
481 with a rhombus in front of a rectangle; (c) Interstitial carbon in Fe lattice (upper) and C-  
482 Fe substitution (lower). The Pauling-Ahrens radii of Fe<sup>0</sup>, Fe<sup>2+</sup>, C<sup>0</sup> are from Ahrens (1952)  
483 and Pauling (1960). The radius of C<sup>4-</sup> is calculated from linear extrapolation of the radii  
484 of O<sup>2-</sup> and N<sup>3-</sup>. The dashed circles represent the radii of Fe<sup>0</sup> and C<sup>0</sup> scaled to the  
485 electronegativity of Fe and C at 2.55 and 1.83, respectively.

486

487 **Figure 7.** The (a) Volume and mass per iron atom, and (b) density of FeC<sub>x</sub>, Fe<sub>3</sub>C, and  
488 Fe<sub>7</sub>C<sub>3</sub> as a function of carbon content. In (b), the gray line is drawn through pure *hcp* Fe  
489 and stoichiometric Fe<sub>3</sub>C. The dotted lines represent densities calculated by assuming  
490 stoichiometric composition. The dashed and solid lines correspond to the densities  
491 calculated by applying the carbon vacancy or C-Fe substitution mechanism, respectively.

492

**Revision 2**

---

493 **Figure 8.** (a) Non-stoichiometry in iron-light element alloys. Open symbols represent  
494 stoichiometric compounds. The radii of light elements and iron are represented by the  
495 circles on the left. The radius of  $C^{4-}$  or  $S^{2-}$  (outer circles) is larger than that of  $C^0$  or  $S^0$   
496 (inner circles), respectively. (b) Density of iron-light-element alloys as a function of light  
497 element concentration. The ranges of non-stoichiometric compositions are denoted by  
498 horizontal bars.  
499

Revision 2

500 **Table 1.** Density of iron-light-element alloys at 1 bar and 300 K.

	Z	Light element		Cell Volume (Å <sup>3</sup> )	Cell Mass (g/mol)	mechanism	density (g/cm <sup>3</sup> )	$\alpha_c^a$ (% per wt.%)	$\alpha_c^{*b}$ (% per wt.%)
		(wt.%)	(at.%)						
$\alpha$ -Fe <sup>c</sup>	2	0	0	23.54	112	-	7.90		
$\gamma$ -Fe <sup>d</sup>	4	0	0	44.83	224	-	8.30		
$\epsilon$ -Fe <sup>e</sup>	2	0	0	22.49	112	-	8.27		
$\gamma$ -FeC <sub>x</sub> <sup>d</sup>	4	0.4	1.2	45.65	224.96	C interstice	8.183	2.5	1.4
		1.8	8	47.24	228.18	C interstice	8.020	1.7	
		5.8	22.3		713.33	C vacancy	7.672	1.3	
Fe <sub>3</sub> C <sup>f</sup> (FeC <sub>0.33±x</sub> )	4	6.7	25	154.39	720	assume stoichiometry <sup>k</sup>	7.744	1.1	-0.9
		6.9	25.6		714.14	substitution	7.664	1.1	
		6.7	25	154.73	720	assume stoichiometry <sup>k</sup>	7.727	0.96	
Fe <sub>7</sub> C <sub>3</sub> <sup>g</sup> (FeC <sub>0.43±x</sub> )	2	8.8	31		847.32	substitution	7.532	1.0	2.6
		8.4	30	186.8(1)	856	assume stoichiometry <sup>k</sup>	7.610	0.93	
		10.3	35		812.17	substitution	7.243	1.2	
		8.4	30	186.2(1)	856	assume stoichiometry <sup>k</sup>	7.634	0.74	
Fe <sub>1-x</sub> O <sup>h</sup>	4	23.1	51.3	79.95	276.8	Fe vacancy	5.749	1.3	2.1
		23.7	52.1	78.95	270.08	Fe vacancy	5.681	1.3	
Fe <sub>1-x</sub> Si <sub>x</sub> <sup>i</sup>	2	5.2	10	22.99	106.4	substitution	7.684	1.4	0.4
		8.1	15	22.63	103.6	substitution	7.601	1.0	
Fe <sub>1-x</sub> S <sup>j</sup>	2	36.4	50	60.36	176	stoichiometric	4.840	1.1	1.6
		38.6	52.4	59.27	166.7	Fe vacancy	4.670	1.1	
		39.5	53.3	57.98	162	Fe vacancy	4.640	1.1	

501 <sup>a</sup> Compositional expansion coefficient with respect to  $\epsilon$ -Fe.

502 <sup>b</sup> Relative compositional expansion coefficient between two compositions with same  
 503 phase. The Fe<sub>1-x</sub>S was calculated based on the stoichiometric FeS with 50 at.% S.

504 <sup>c</sup> Hull (1917).

505 <sup>d</sup> Okamoto (1992). The density of  $\gamma$ -Fe at 300 K was extrapolated from data at high  
 506 temperature, where it is stable.

507 <sup>e</sup> Fei et al. (2016). The density of  $\epsilon$ -Fe was extrapolated from data at high pressure, where  
 508 it is stable.

509 <sup>f</sup> Walker et al. (2013).

510 <sup>g</sup> this study.

511 <sup>h</sup> Hazen and Jeanloz (1984).

512 <sup>i</sup> Machová and Kadečková (1977) and Routbort et al. (1971).

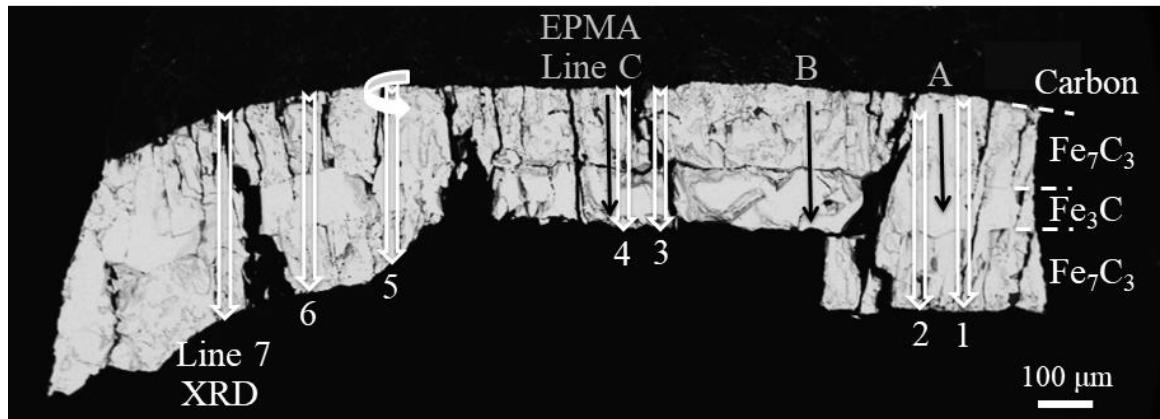
513 <sup>j</sup> Koto et al. (1975) and Nakano et al. (1979).

514 <sup>k</sup> **Incorrect density calculation using unit-cell mass from stoichiometric formula and unit-**  
 515 **cell volume from non-stoichiometric sample.**



Revision 2

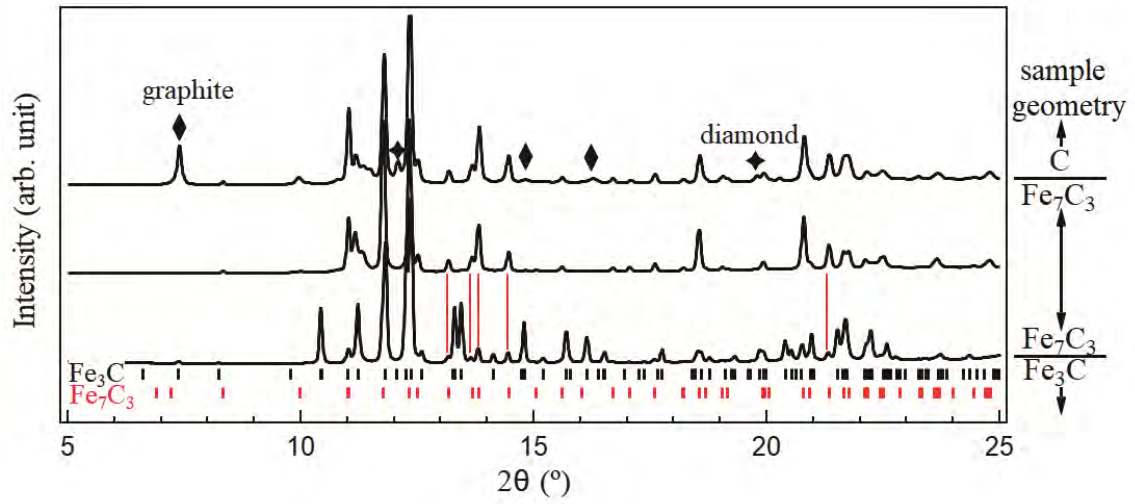
Figure 1



516  
517

Revision 2

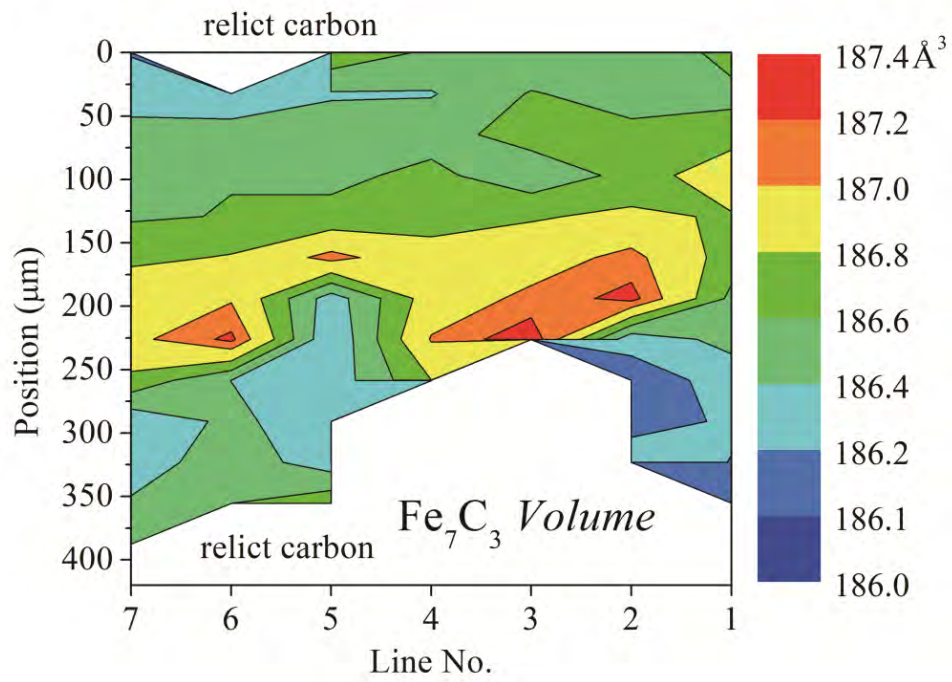
Figure 2



518  
519

Revision 2

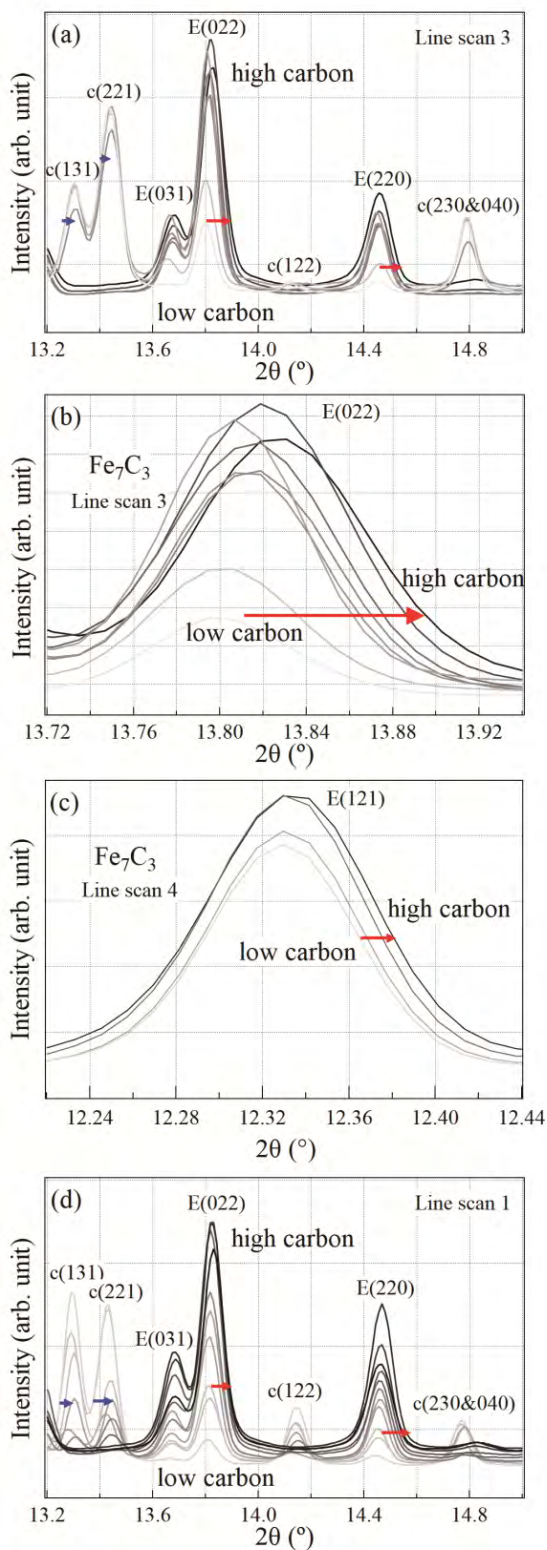
Figure 3



520  
521

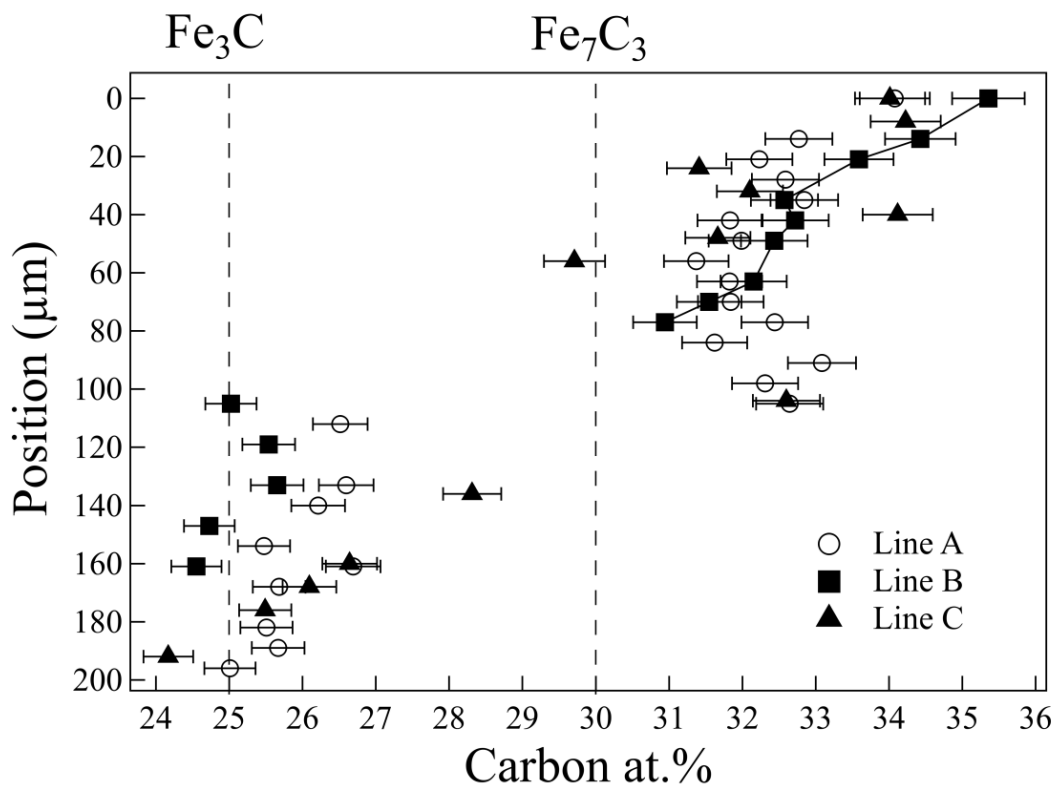
Revision 2

Figure 4



522  
523

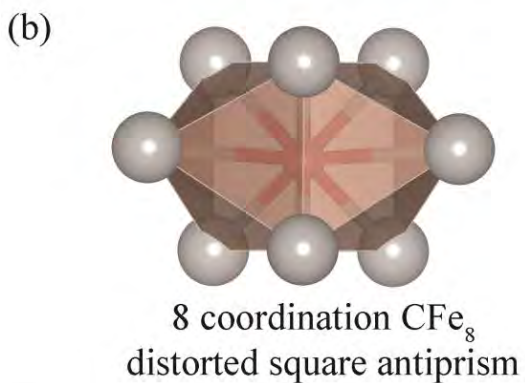
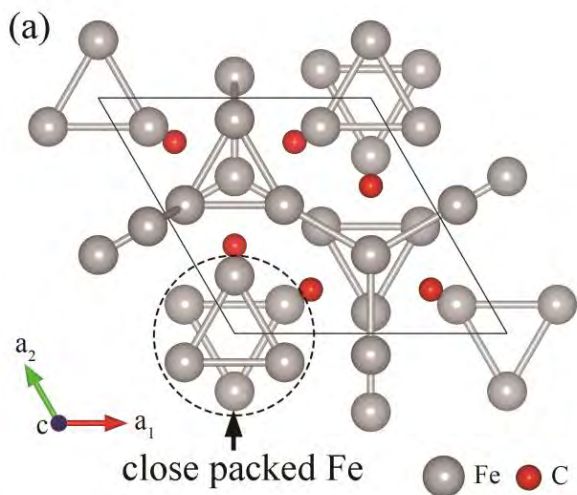
Figure 5



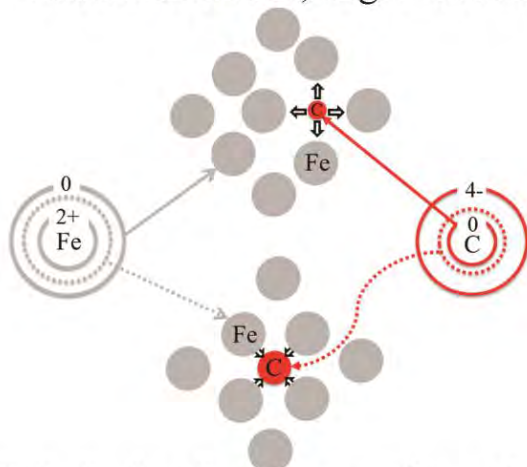
524  
525

Revision 2

Figure 6



(c) Interstitial carbon, larger volume

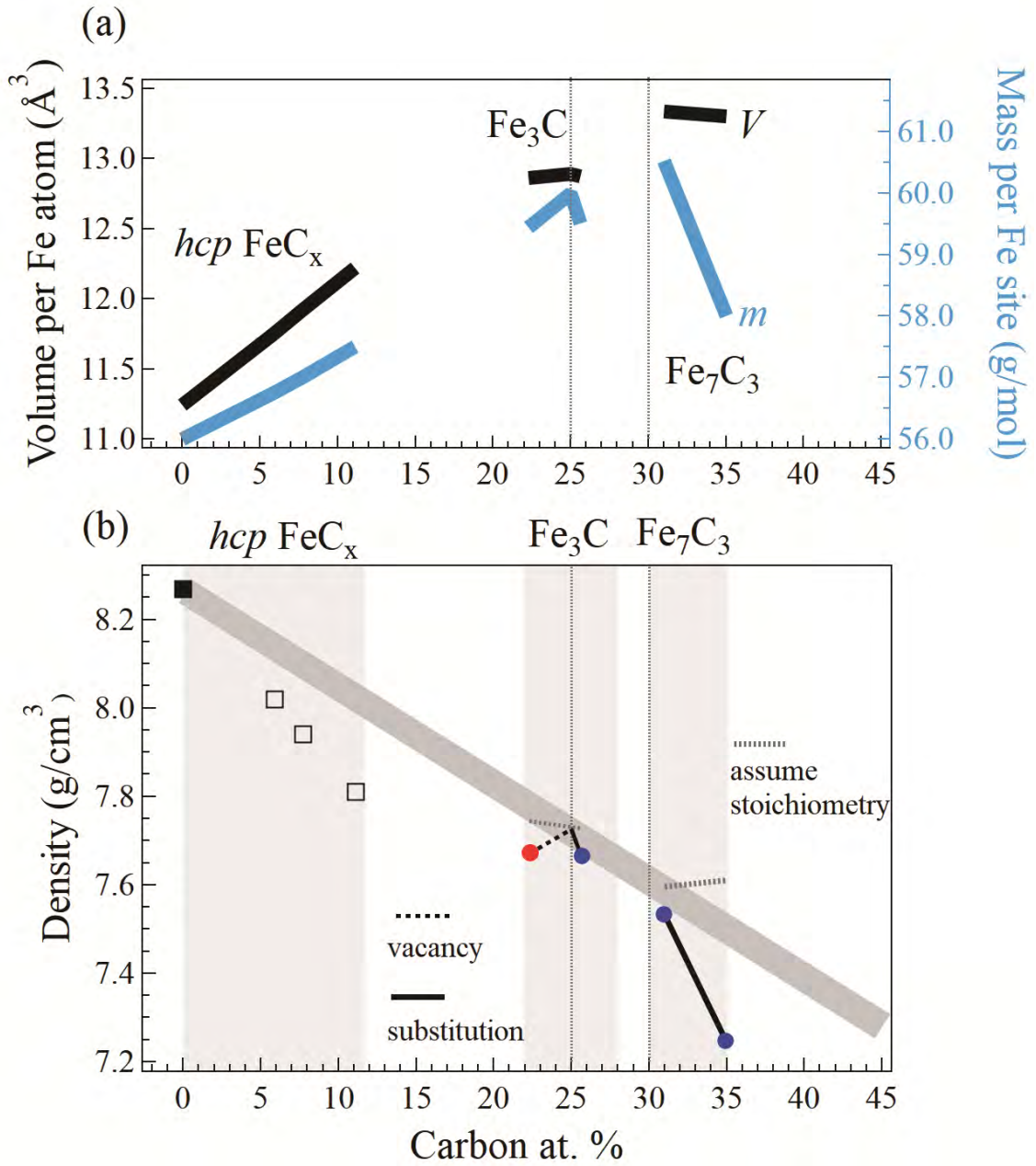


Substitutional carbon, smaller volume

526  
527

Revision 2

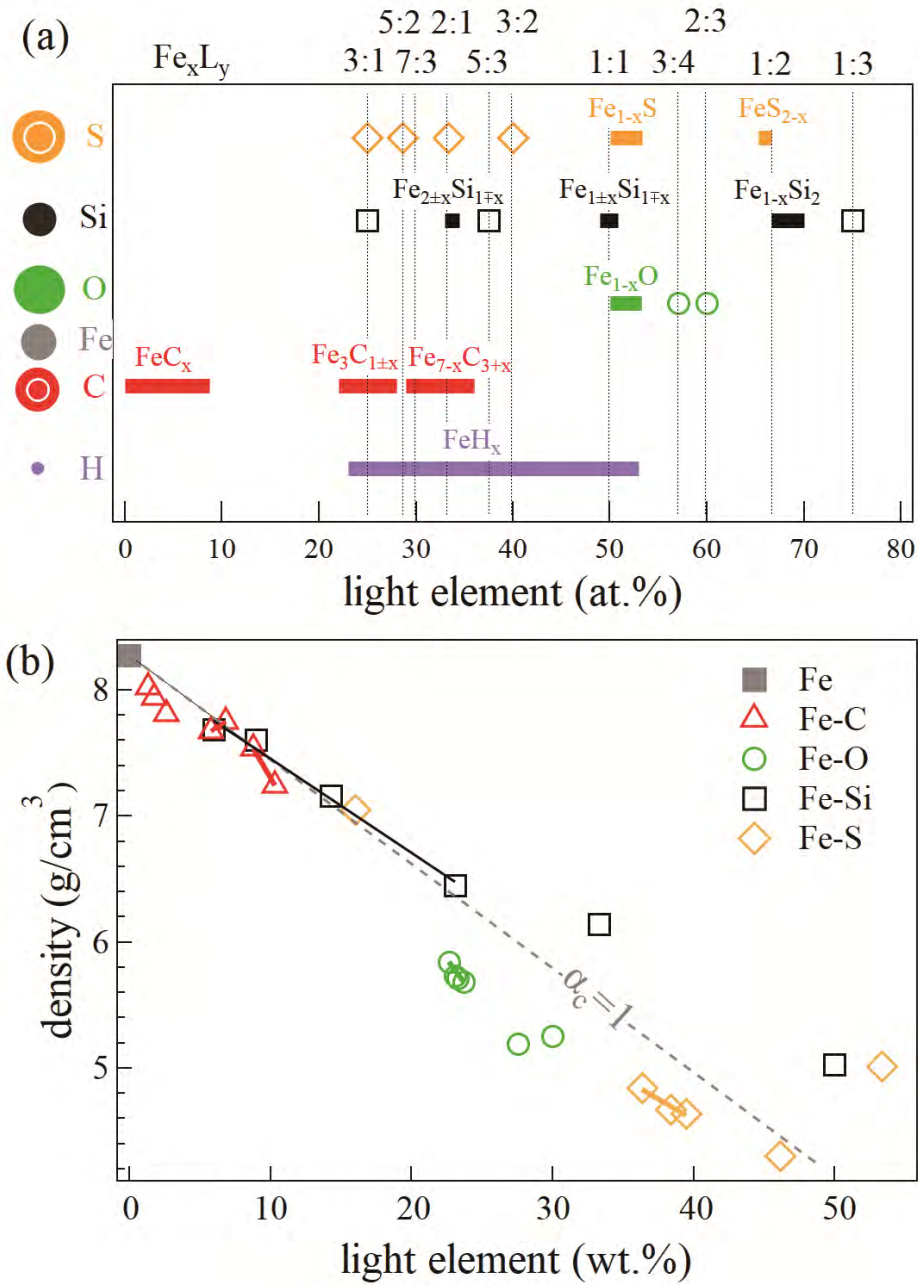
Figure 7



528  
529

Revision 2

Figure 8



530  
531